Mechanism of geometric nonlinearity in a nonprismatic and heterogeneous microbeam resonator

Keivan Asadi,[1] Junfeng Li,[1] Snehan Peshin,[2] Junghoon Yeom,[2] and Hanna Cho[1,*]
[1]*Department of Mechanical and Aerospace Engineering, The Ohio State University, Columbus, Ohio, USA*
[2]*Department of Mechanical Engineering, Michigan State University, East Lansing, Michigan, USA*
(Received 14 March 2017; revised manuscript received 24 August 2017; published 13 September 2017)

Implementation of geometric nonlinearity in microelectromechanical systems (MEMS) resonators offers a flexible and efficient design to overcome the limitations of linear MEMS by utilizing beneficial nonlinear characteristics not attainable in a linear setting. Integration of nonlinear coupling elements into an otherwise purely linear microcantilever is one promising way to intentionally realize geometric nonlinearity. Here, we demonstrate that a nonlinear, heterogeneous microresonator system, consisting of a silicon microcantilever with a polymer attachment exhibits strong nonlinear hardening behavior not only in the first flexural mode but also in the higher modes (i.e., second and third flexural modes). In this design, we deliberately implement a drastic and reversed change in the axial vs bending stiffness between the Si and polymer components by varying the geometric and material properties. By doing so, the resonant oscillations induce the large axial stretching within the polymer component, which effectively introduces the geometric stiffness and damping nonlinearity. The efficacy of the design and the mechanism of geometric nonlinearity are corroborated through a comprehensive experimental, analytical, and numerical (finite element) analysis on the nonlinear dynamics of the proposed system.

DOI: 10.1103/PhysRevB.96.115306

I. INTRODUCTION

Many microelectromechanical systems (MEMS) employ mechanical resonators, often fabricated into a beam-type structure from novel materials such as nanotubes, graphenes, crystalline silicon, etc. The high structural quality of those materials combined with the reduced effective mass allows such beams to operate at very high resonance frequencies with extremely high Q factors (i.e., low damping). These beneficial attributes provide the basis for exceptional performance of MEMS applications such as extremely sensitive sensors [1–4], mechanical energy harvesters [5–7], nano/microrelays [8,9], logic memory and computation [10–12], field effect transistors [13], and a high frequency reference in oscillators [14–16]. The MEMS devices implemented in these applications were mostly designed to operate in their linear resonant modes with the aforementioned benefits. Mechanical resonators at the micro/nanoscale, however, can easily transit from linear to nonlinear resonances because of its remarkable properties of small size and low damping. Whereas the absolute magnitude of the involved resonance is small, the relative magnitude of the oscillation amplitude can be substantially large compared to the reduced device size owing to their high Q factor. As a result, the significant abatement of linear dynamic operational range renders linear operational displacements to be restricted to an extremely small magnitude, which is often comparable to the noise level [17]. Thereby performance and practical applications of MEMS resonators are often limited by difficulties in transduction of miniscule displacements and requirements of impractical environments, such as extremely low temperature and pressure to reduce the noise.

In order to overcome the limitation of linear MEMS resonators, recent efforts have been devoted to design MEMS devices that implement [18] or harness nonlinearity [19]. Utilization of intentional geometric nonlinearity in MEMS has proved to achieve higher bandwidth resonances, frequency tunability, and instantaneous hysteresis switching that are difficult to attain in a linear setting. One of the commonly used applications of nonlinear microresonators is in sensing. Cho *et al.* [20] developed a highly sensitive mass sensor by employing geometric nonlinearity in a fixed-fixed nanotube in which the sensor performance could be improved by utilizing nonlinear instability. Venstra *et al.* [21] developed a microcantilever based gas sensor where the frequency shift due to adsorption and desorption in the nonlinear regime is larger by a factor of three compared to operating in the linear regime. Researchers have also recently taken advantage of nonlinear characteristics such as internal resonance [14], parametric feedback [22], and bifurcation topology amplification [23] in suppressing phase noise level to improve oscillator performance by overcoming the operational limits due to thermal noise [17,24,25]. Another significant application of nonlinear microresonators is in developing mechanical memory devices and logic gates where coexistence of two stable states enables switching of the output logic values [10,11,26,27].

Considering these applications of nonlinear microresonators, the ability to manipulate the level of nonlinearity is beneficial to explore their targeted nonlinear behaviors. In the recent years, substantial efforts have been put forth to tailor the strength of structural nonlinearity [18,28,29]. Saghafi *et al.* [28] provided an analytical scheme based on a continuous system model to predict the onset of nonlinearity in a bilayer clamped-clamped microbeam to enhance the working dynamic range. Dou *et al.* [18] established a systematic numerical approach combined with the optimization technique to maximize or minimize objective nonlinearity in a clamped-clamped beam by varying its thickness profile. Li *et al.* [30] experimentally verified the efficacy of the optimized design in which the nonlinear coefficient can be altered from threefold increase to twofold decrease by optimizing the thickness profile.

*Corresponding author: cho.867@osu.edu

In contrary to previous resonator designs based on simple homogeneous and/or prismatic beam type resonators, a heterogeneous and nonprismatic design provides more freedom to control the targeted level of nonlinearity and to provide rich nonlinear behaviors. For example, authors' previous works have successfully introduced strong geometric nonlinearity by coupling a nanoscale structure such as a boron nitride (BN) nanotube [31,33] or a silicon nanomembrane [32] into a silicon microcantilever. However, these systems require the manual integration of nanotube and nanomembrane, and, thereby, they are not practical to be integrated into the batch-fabricated MEMS devices. The difficulties in the fabrication also limit the room to adjust the structural dimensions of the system to provide the optimal nonlinearity. Moreover, the assumptions used to simplify the actual system into a theoretical model have never been validated in detail.

In the current paper, we consider a nonprismatic, heterogeneous microbeam structure, comprised of a silicon microcantilever with a polymer coupling. We developed the batch fabrication process that enables the integration of two dissimilar materials (e.g., silicon and polyimide) in a free-standing fashion. Owing to the feasibility in controlling the structural dimension and material properties, the beam could be intentionally designed to exhibit a drastic change in the stiffness between two materials, which has been confirmed to be the basis of strong geometric nonlinearity. A comprehensive experimental, analytical, and numerical analysis is applied to understand the origination of geometric nonlinearity in the design. Especially the finite element analysis (FEA) is employed as a strong complementary approach to experimental characterization and analytical modeling, to provide detailed dynamic responses throughout the structure during nonlinear resonances.

II. SYSTEM DESCRIPTION AND FABRICATION

The scanning electron microscope (SEM) image of the microcantilever-polymer system is depicted in Fig. 1(a). The system consists of a silicon (Si) microcantilever bridged to a firm ground by a polymer (polyimide) attachment. The length, width, and thickness of the Si cantilever are $L_1 = 500\,\mu$m, $b_1 = 100\,\mu$m, and $t_1 = 2\,\mu$m; those of the polymer attachment are $L_2 = 50\,\mu$m, $b_2 = 12\,\mu$m, and $t_2 = 3\,\mu$m. Subscripts 1 and 2 denote the Si cantilever and polymer attachment, respectively. In this design, we intentionally implement a drastic change in the stiffness between the Si cantilever and polymer attachment by varying the geometrical dimensions (i.e., length and cross-sectional area) and material (i.e., Young's modulus) of the beam structure. As a result, the ratio of effective *bending* stiffness between the Si cantilever (1) and polymer attachment (2) is $k_{\text{bending},1} : k_{\text{bending},2} = 0.18 : 1$, and the ratio of effective *axial* stiffness between these two components is $k_{\text{axial},1} : k_{\text{axial},2} = 40 : 1$. Note that this nonprismatic, nonhomogeneous structural design not only results in a large discrepancy in the effective stiffness between the Si cantilever and polymer attachment but also gives an opposite trend in the magnitude ratio of the bending and axial terms. Thus, in a two-dimensional planar motion of this beam, the bending force induces a relatively larger bending deflection in the Si cantilever part due to its lower bending stiffness, while the axial force mainly stretches the polymer attachment due to its lower axial

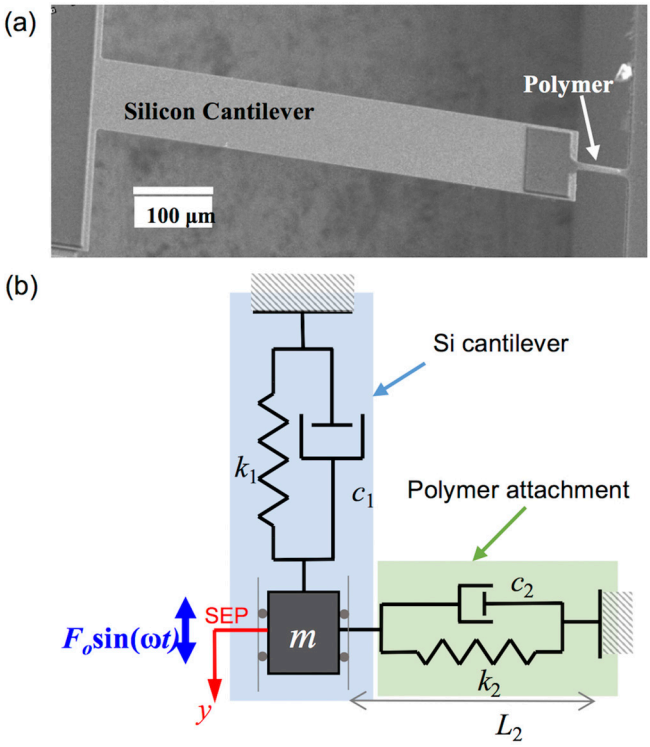

FIG. 1. (a) The SEM image of the system**.** The system consists of a silicon micro cantilever (dimensions: $500\,\mu\text{m} \times 100\,\mu\text{m} \times 2\,\mu\text{m}$) bridged to the ground by a polymer attachment (dimensions: $50\,\mu\text{m} \times 12\,\mu\text{m} \times 3\,\mu\text{m}$). (b) A lumped parameter model of the system. A flexural displacement of the microcantilever is modeled by a linear spring (k_1), linear damping (c_1), and mass (m), which is constrained by a horizontal spring (k_2) and damper (c_2). The large vertical motion of the mass renders stretching in the polymer component so that the global dynamics switches from linear to nonlinear hardening.

stiffness. In other words, when this microcantilever-polymer system is driven to oscillate near one of its mode frequencies, a large *vertical, bending displacement* of the free end of Si cantilever relative to the neutral position induces the *axial stretching of the polymer bridge*, which effectively accomplishes the intentional geometric nonlinearity in this design.

The device was fabricated by the batch process based on the standard MEMS fabrication combined with a modified soft lithographic technique [34]. The detailed process sequence is explained elsewhere [35]. Briefly, a pattern of microcantilever was formed in a silicon-on-insulator (SOI) wafer using a conventional photolithography technique and reactive ion etching (RIE). Then, a thin polymer layer (Polyimide, PMDA-ODA) was blanket transferred to the Si device layer and patterned by applying an additional photoresist film. Etching was then performed to reveal the suspended polymer layer suspended over the gap. Finally, a backside inductively-coupled plasma deep RIE (ICP-DRIE) was performed to release the free-standing microcantilever-polymer system. In contrast to the previous works in Refs. [31–33], where the nonlinear attachments (i.e., the BN nanotube) were manually integrated in a one-by-one and strenuous fashion, the proposed device was manufactured by a massively parallel, scalable process, suitable for the practical MEMS applications.

III. ANALYTICAL MODELING

Considering this dynamic configuration of the structure, we can simplify the nonlinear microcantilever-polymer system based on the lumped parameter model shown in Fig. 1(b). The Si microcantilever is modeled as a damped, linear harmonic oscillator with mass (m), viscous damper (c_1), and spring (k_1). The vertical bending motion of the Si cantilever is modeled as a vertical displacement of the lumped mass m about the static equilibrium position (SEP) in this lumped model, resulting *in the linear compression and tension* within the vertical spring during oscillations. Due to its smaller dimension and density, the mass of polymer is considered to be negligible (cf., $m_1 \approx 233$ ng, $m_2 \approx 2$ ng). Instead, its storing and dissipative forces are modeled as horizontally attached linear spring (k_2) and damper (c_2), based on the Kelvin-Voigt model. The damping in the polymer emerges from the viscoelastic properties of the polymer at high strain rates [33]. The horizontal arrangement of the polymer in the model will eventually simulate the geometric nonlinearity due to the axial stretching within the polymer attachment. It is important to note that the horizontal spring is subject to *tension only*, when the mass is vertically displaced from the SEP either in the positive or negative direction (i.e., $+y$ or $-y$), assuming that the horizontal spring is in its unstretched length (L_2) at the SEP. The validity of these assumptions will be later supported by the numerical simulations. Finally, the harmonic excitation force is modeled to be directly applied to the mass m, even though the base excitation using a piezoelectric actuator is employed in the experiment. Our previous works confirmed that this simplification is valid when the dissipative forces are much smaller than the restoring terms, as for microscale structures in a vacuum environment [32,33].

The governing equation of this model can be obtained by performing the balance of vertical forces applied to the lumped mass m when it is displaced vertically from the SEP. With a vertical displacement of y, the horizontal spring and damper undergoes the force of $k_2\delta + c_2\dot{\delta}$ where $\delta = \sqrt{{L_2}^2 + y^2} - L_2$. The vertical component of this force can be expressed as $\frac{k_2}{2{L^2}_2}y^3 + \frac{c_2}{{L^2}_2}y^2\dot{y}$ after the terms beyond the third order are truncated with an assumption of a small vertical displacement compared to L_2 (i.e., $y/L_2 \ll 1$). Then the governing equation of this system can be written as

$$m\ddot{y} + c_1\dot{y} + k_1 y + k_3 y^3 + c_3\dot{y}y^2 = F_o \sin\omega t$$
$$k_3 = \frac{k_2}{2{L^2}_2}, \quad c_3 = \frac{c_2}{{L^2}_2} \tag{1}$$

Equation (1) is a Duffing equation with cubic nonlinear stiffness and damping terms both originating from axial deformations in the horizontal spring (i.e., polymer attachment), which is of a pure geometrical origin. We can proceed to find the steady state solution by normalizing Eq. (1),

$$\bar{y}'' + (2\zeta_1 + {\zeta_2}^2\bar{y}^2)\bar{y}' + \bar{y} + \alpha\bar{y}^3 = \bar{f}\sin\Omega\tau$$
$$\bar{y} = \frac{y}{L_1}, \quad \omega_0 = \sqrt{\frac{k_1}{m}}, \quad \tau = \omega_0 t, \quad \zeta_1 = \frac{c_1}{2m\omega_0},$$
$$\zeta_2 = \frac{c_3}{m\omega_0}{L_1}^2 \quad \Omega = \frac{\omega}{\omega_0}, \quad ()' = \frac{d}{d\tau}, \quad \bar{f} = \frac{F_o}{k_1 L_1}. \tag{2}$$

Introducing a small scale parameter ε, we rescale Eq. (2) according to $\bar{y} \to \sqrt{\varepsilon}\bar{y}$, $\zeta_1 \to \varepsilon\zeta_1$, and $\bar{f} \to \sqrt[3]{\varepsilon^2}\bar{f}$. The method of multiple scales is utilized to derive the steady state response, assuming that the response is expressed in two time scales. A set of autonomous modulation equations are obtained after inserting the complex amplitude into the modulation equation as

$$a' = -\zeta_1 a - \frac{\zeta_2}{8}a^3 + \frac{\bar{f}}{2}\cos\gamma$$
$$a\gamma' = a\sigma - \frac{3}{8}\alpha a^3 + \frac{\bar{f}}{2}\sin\gamma \tag{3}$$
$$\gamma = \sigma T_1 - \beta,$$

where a and β are real valued amplitude and phase as a function of slower time scale $T_1 = \varepsilon\tau$. σ is the frequency detuning parameter defined as $\sigma = \Omega - 1$. The relation between steady state amplitude and frequency is derived by setting $a' = \gamma' = 0$ in Eq. (3),

$$\left[(\zeta_{\text{eff}})^2 + \left(\sigma - \frac{3}{8}\alpha {A_{\text{ss}}}^2\right)^2\right] = \frac{\bar{f}^2}{4}$$
$$\zeta_{\text{eff}} = \zeta_1 + \frac{\zeta_2}{8}{A_{\text{ss}}}^2, \tag{4}$$

where A_{ss} is the steady state amplitude and ζ_{eff} is the overall damping accounting for both the constant, linear viscous damping (ζ_1) and the amplitude-dependent, nonlinear damping ($\zeta_2 A_{\text{ss}}^2/8$). Equation (4) leads into the so-called backbone curve equation by taking the values of the damping and forcing terms as zeros, i.e., $A_{\text{ss}} = (\frac{8\sigma}{3\alpha})^{0.5}$, which directly relates the frequency to the steady state amplitudes with the nonlinear coefficient.

IV. EXPERIMENTAL RESULTS

The experimental setup consists of three main parts for device actuation, dynamic response measurement, and data acquisition parts. The experiment is designed in a way to mitigate sources of nonlinear mechanisms related to actuation and detection such that the origin of nonlinearity is purely from the structure. A piezoelectric shaker was employed to actuate the microstructure system from the base. Since the piezoelectric shaker was carefully selected to avoid its own resonance near the excitation frequencies, the nonlinearity related to excitation can be considered negligible, making the assumption of a linear harmonic excitation valid. The shaker was excited by applying ac voltage at peak-to-peak voltage amplitudes (V_{pp}) ranging from 0.1 V to 20 V by a waveform generator (Tektronix AFG3022c). The dynamic response of a device was measured via a laser Doppler vibrometer (LDV; Polytec OFV-534 sensor and OFV-5000 controller), while the laser light was focused near the point where the cantilever exhibited the maximum vertical displacements. The measured signal delivered to a remote computer through an oscilloscope (Tektronix DSOX4034A) was analyzed to produce the frequency spectrum of the response. The device was located in a vacuum environment with an absolute pressure of 5 mTorr to reduce the effects of air damping loss on the response.

As the first step, we obtained the linear modal frequencies by measuring thermomechanical spectrum from the microcantilever. Then the excitation frequency was swept around the

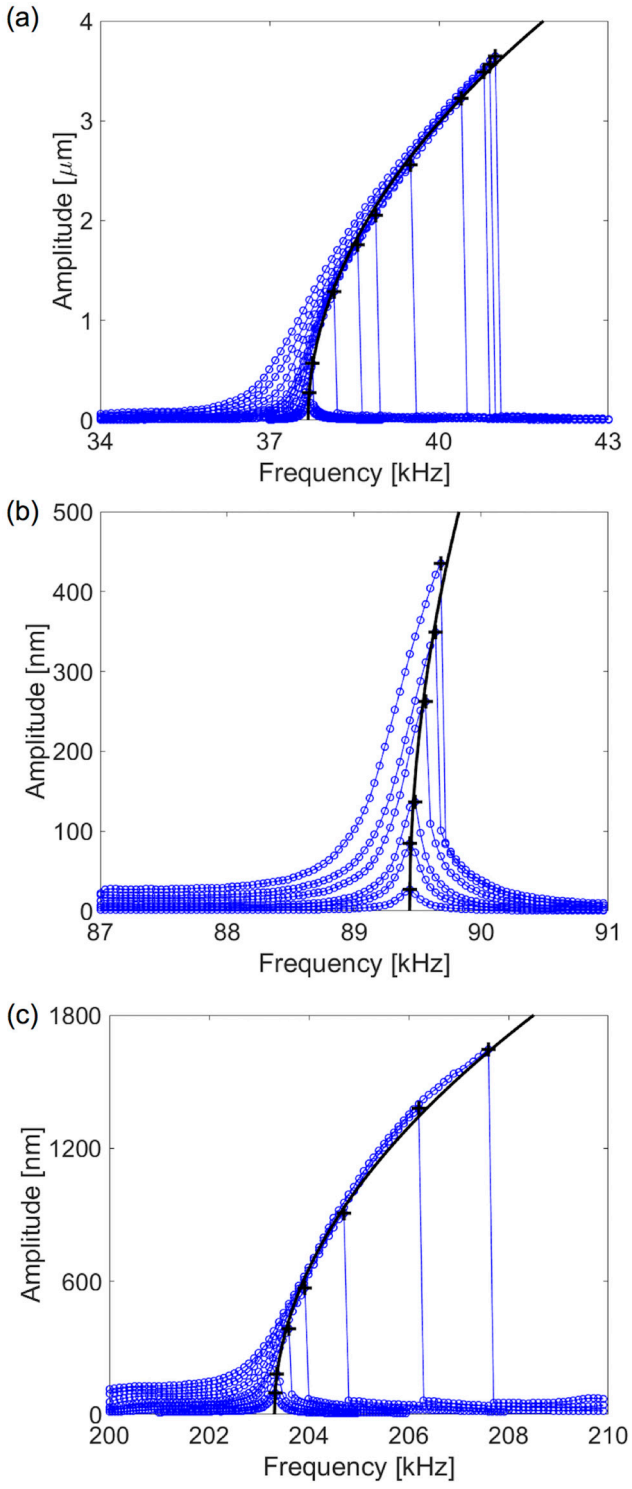

FIG. 2. Nonlinear hardening responses at the (a) first mode, (b) second mode, and (c) third mode. Experimentally acquired frequency responses at different base excitation voltages (in blue circle). At high driving voltages, tension is introduced in the midplane of the polymer structure; therefore, cubic nonlinearity dominates the system dynamics. As the driving amplitude increases, the resonant frequency increases, and thereby, the resonance curve bends toward higher frequencies. The backbone curves are fitted to the maximum of the frequency responses (in black) to obtain the nonlinear coefficients and linearized resonant frequencies.

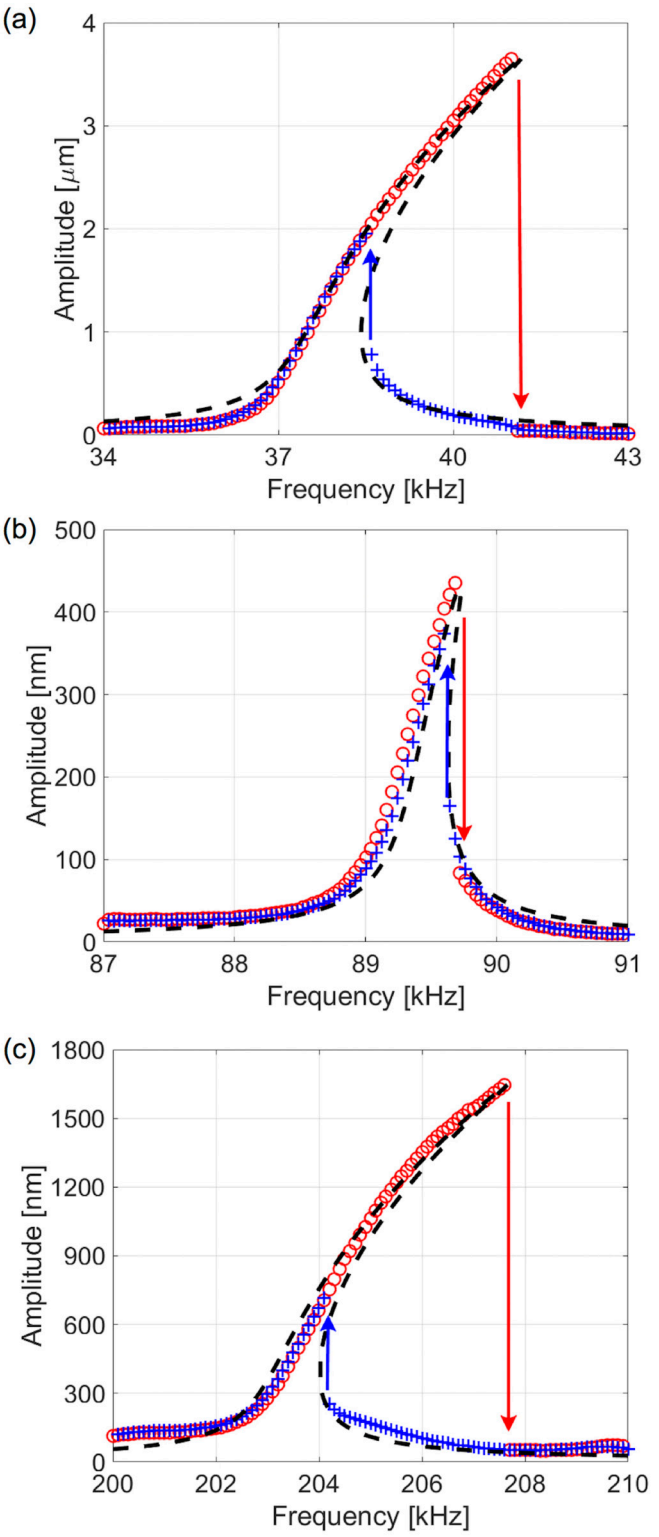

FIG. 3. Nonlinear hysteresis phenomenon at the (a) first mode, (b) second mode, and (c) third mode. The responses during sweeping up and down the excitation frequency are plotted in red circles and blue crosses, respectively. There is a region of bi-stability between drop-down and jump-up frequencies shown in arrows. The analytical predictions (in dashed black curves) are fitted on the experimentally measured frequency responses, which agree well with the experimental responses.

linear resonant frequency while fixing the excitation voltage of V_{pp}. The oscillation amplitude at each excitation frequency was obtained from the displacement frequency spectrum completed by fast Fourier transforming of the integrated velocity signal from the LDV. This step was repeated at different levels of V_{pp} around the mode of interest. When we observed the nonlinear behavior during the upward frequency sweep at high V_{pp}, we repeated the measurement as the frequency was swept downward to capture the nonlinear hysteresis. Through the experimental characterization of the system, we observed clear hardening resonances in all of the first three bending modes. Figures 2(a)–2(c) show the experimentally measured response spectrums in the first, second, and third flexural modes, respectively (cf. blue curves and circles). In Fig. 2, the gradual transition from linear to nonlinear responses with the increase of the excitation voltage illustrates that the cubic nonlinear stiffness term as a result of stretching of the polymer component starts to affect the global dynamics of the whole structure as the amplitude of oscillations increases beyond a certain amplitude. Note that this stiffness hardening effect effectively introduces nonlinear dynamics into the first three flexural modes. Since the resonant frequency increases as the oscillation amplitude is increased due to the nonlinear effect, the resonant bandwidth expands over a wider frequency range compared with the bandwidth of a corresponding linear system. The bandwidth depends not only on the strength of nonlinearity but also on the excitation force level, which confirms the frequency tunability. However, the resonant bandwidth is also limited by nonlinear damping, which increases with the oscillation amplitude as well. Figures 3(a)–3(c) show a nonlinear hysteresis phenomenon. The responses during the upward and downward frequency sweeps are presented by red circles and blue crosses, respectively. This hysteresis phenomenon indicates that there exists more than one stable branch over a frequency range so that the realized nonlinear responses are not identical, depending on the frequency sweep direction. While the frequency is swept upward, the response follows the upper stable branch, followed by an abrupt drop to the lower stable branch at the drop-down frequency. The branch selection is reversed while the frequency is swept down: The response stays in the lower branch up to the jump-up frequency at which the response suddenly jumps to the upper branch.

The analytical model is first validated by the experimental results. The backbone curve (black line) was first obtained in Fig. 2 by fitting the maximum displacements of the experimentally acquired nonlinear frequency responses at different excitation levels (black crosses). The linearized resonant frequency (ω_o) and nonlinear stiffness coefficient (α) of each mode are obtained to give the best fitting of the backbone curve to the experimental data. Given these values, the whole frequency spectrums in Fig. 3 were fitted to Eq. (4) to find the effective damping ratio ζ_{eff} and the equivalent excitation force ($\bar{f}$). The frequency responses predicted by the analytical model using these estimated parameters were plotted by the dashed lines in Fig. 3, which almost perfectly agrees with the experimental results. As shown in Eq. (4) the effective damping ζ_{eff} is dependent on the oscillation amplitude (A_{ss}). We estimated the linear damping ratios (ζ_1) from a linear frequency response with a small resonant amplitude below the critical amplitude exhibiting the onset of the nonlinearity. All parameters obtained by the analytical model are listed in Table I for the first three bending modes.

TABLE II. Material properties used in FE simulation.

	Young's Modulus (GPa)	Density (kg/m^3)	Poisson's Ratio
Silicon	180	2330	0.28
Polymer	3	1400	0.34

V. FINITE ELEMENT SIMULATION

We also performed the FEA using ABAQUS 6.14 (Hibbit Inc., Providence, Rhode Island) to better understand the nonlinear mechanism observed in the microcantilever-polymer structure. The procedure of FEA to obtain the nonlinear dynamic response is described in Fig. 4. The material properties used for this numerical simulation are provided in Table II. We modeled the three-dimensional (3D) structure of the system, as seen in its SEM image [cf. Fig. 1(a)], with the boundary conditions taken as clamped-clamped. The structure was properly meshed with reduced order quadratic hexagonal elements to accurately model a thin beam in bending. As a first step, we performed the linear modal analysis to get the linearized mode frequencies and mode shapes of the structure [cf. the inset of Fig. 4(b)]. The simulated linearized resonant frequencies showed a good agreement with the experimentally obtained frequencies in all three flexural modes with the maximum discrepancy less than 3.6%, as provided in Table I.

TABLE I. Comparison between experiment results and FE simulated results in the first three bending modes.

		Flexural Mode Number		
		1	2	3
Linearized resonant frequency	Experiment [kHz]	37.6	89.5	203.4
	Simulation [kHz]	36.5	86.4	199.1
	Relative difference (%)	3.01	3.59	2.16
Nonlinear coefficient (α)	Experiment	414.8	1041.4	473.4
	Simulation	463.4	806.8	493.0
	Relative difference (%)	11.72	29.07	4.14
Quality factor	Linear $Q_{linear} = 1/(2\zeta_1)$	675	880	1100
	Effective $Q_{eff} = 1/(2\zeta_{eff})$	140	630	900

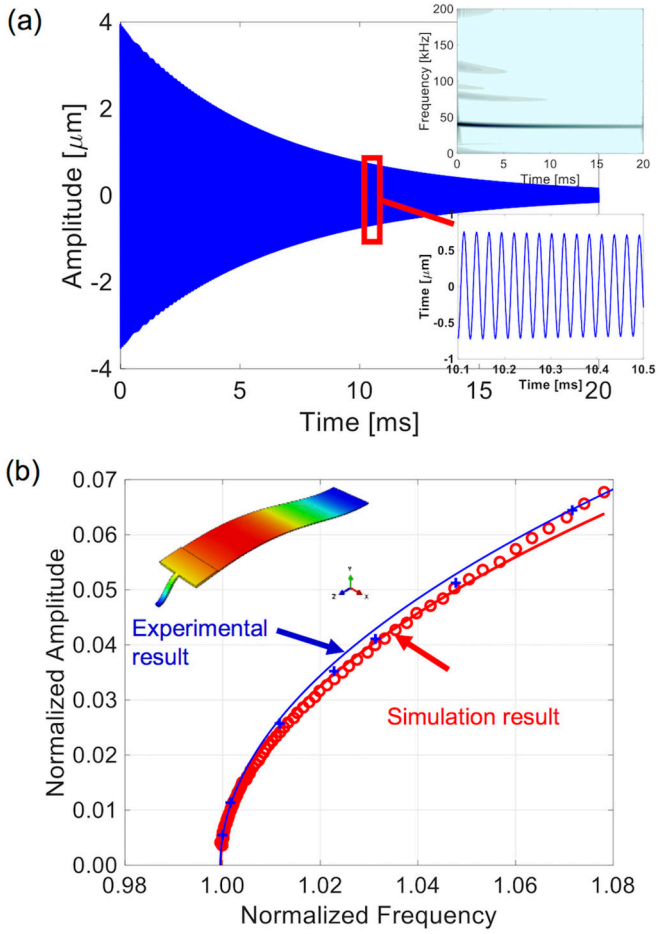

FIG. 4. The FEA results at the first mode. (a) A free decay time response after releasing from a large deflection corresponding to its first mode. The wavelet transform of the response in the upper inset shows that the first mode is dominantly excited. A magnified portion of the time response is shown in the lower inset figure. (b) A nonlinear amplitude-frequency dependence calculated from the FEA time response (in red) is compared with the experimental backbone curve (in blue). The comparison shows a perfect match between FE simulation and experimental results. The first mode shape of the system is illustrated in the inset figure.

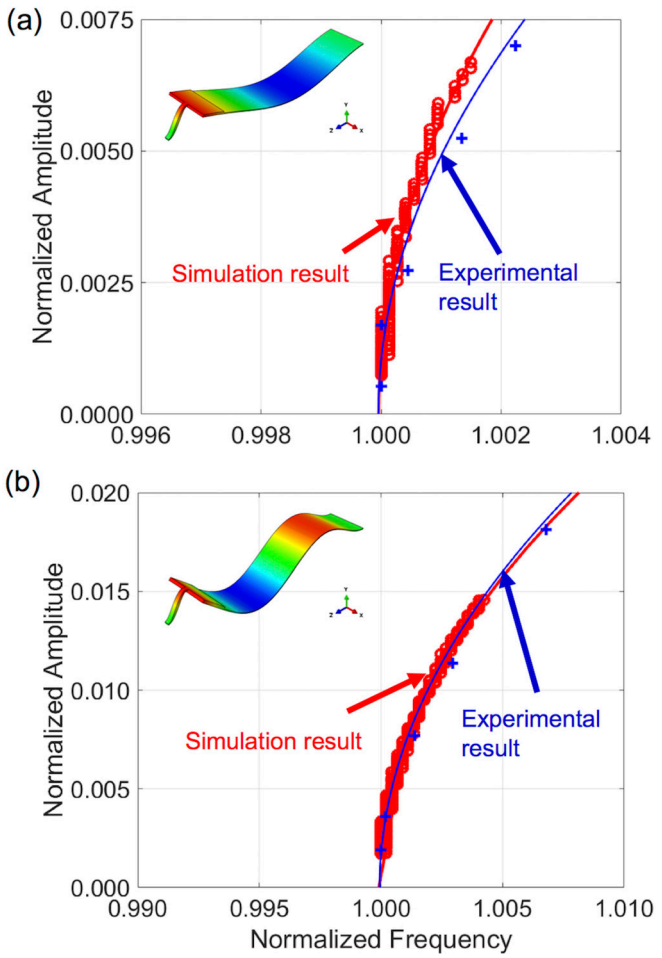

FIG. 5. Experimentally obtained (blue) and FE simulated (red) backbone curves at the (a) second mode and (b) third mode. A nonlinear amplitude-frequency dependence calculated from the FEA time response (in red) shows an excellent agreement with the experimental backbone curve (in blue). The linear mode shapes of the second and the third mode of the system are illustrated in the inset figure.

Then, the dynamic time response of this system was simulated when the structure was released from a sufficiently large initial deflection corresponding to the associated mode shape. The goal of this dynamic analysis was to obtain the nonlinear amplitude-frequency dependency while a flexural mode of interest was excited by applying its mode shape as an initial condition. Simulating the decaying time responses, one can extract the backbone curve from time responses by calculating the resonant frequencies from the successive time periods of oscillations. Figure 4(a) shows the simulated time response of the system at the point of maximum deflection in the Si micro-cantilever when the first flexural mode is excited. As seen in the wavelet transformed results [cf. the upper inset of Fig. 4(a)], the time-frequency representation of the signal, the excited first mode is dominantly exhibited in the simulated dynamics, while the higher modes are slightly excited. We speculate that the discrepancy between the nonlinear and linear mode shapes can slightly excite other modes. Finally, the frequencies of oscillation were calculated at varying oscillation amplitudes to find the frequency-amplitude relationship in Fig. 4(b). The comparison of FE simulation (circle) and experiment (cross) backbone curves at the first, the second, and the third modes are shown in Figs. 4(b) and 5(a)–5(b), respectively, which clarifies that the two plots agree surprisingly well with each other. The numerically obtained nonlinear coefficients listed in Table I also show a good agreement with the coefficients obtained from the experimental results for all of the first three flexural modes with errors less than 30%.

Figure 6 illustrates the linear mode shapes of the first three flexural modes simulated by FEA. As we intended in the micromechanical resonator design by setting drastic, reversed stiffness arrangements between silicon and polymer component, large vertical bending displacements are achieved at the end of the silicon cantilever in all three modes, which induces the large axial stretching in polymer component. It verifies the effective implementation of geometric nonlinearity in our

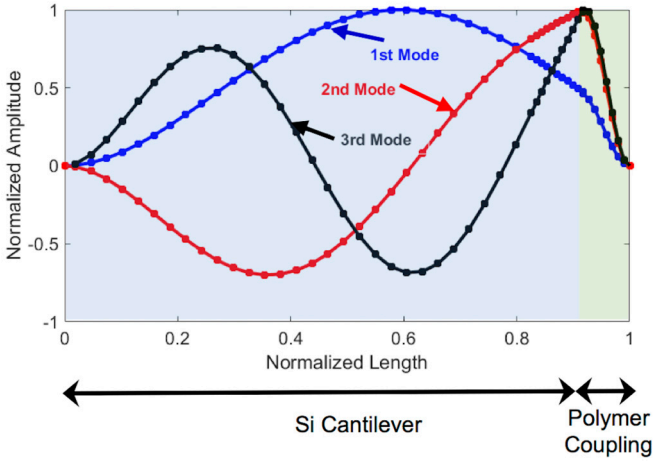

FIG. 6. The FE simulated linear mode shapes of the first three flexural modes: The mode shapes illustrates that large bending displacements in the silicon microcantilever induce axial stretching in polymer coupling.

nonlinear design. To further justify the design, we investigated the effect of stiffness parameters on the resulting nonlinearity, as summarized in Fig. 7 and Table III. We performed FE simulation for the fundamental mode of the same structure while fixing the geometry and all material properties other than the Young's modulus in the nonlinear coupling element (i.e., polymer component). The resulting frequency-amplitude dependence curves (i.e., nonlinear backbone curves) are provided in Fig. 7 when Young's modulus is varied from 1 MPa to 60 MPa. As estimated in Table III, as the material of the nonlinear coupling element gets stiffer, the difference in axial stiffness between the two components is reduced. Thereby, the nonlinear component is less likely to stretch at the same level of excitation, and thus, the resulting Duffing nonlinearity is diminished. Besides, the simulation results show that the validity of the proposed model is limited to a range of material stiffness: As Young's modulus exceeds some threshold value, the global dynamics switches to softening and the proposed analytical model is no longer valid.

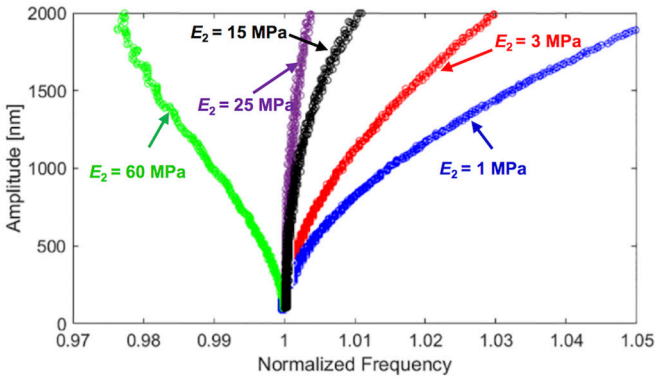

FIG. 7. Simulated nonlinear frequency-amplitude curves for different values of Young's modulus in the nonlinear component. It is clear that an increase in Young's modulus of the coupling component reduces the effective Duffing coefficient. The effect of Young's modulus on the stiffness ratios and nonlinear coefficients is summarized in Table III.

TABLE III. Stiffness ratios between the two structural components and resulting nonlinear coefficients simulated in Fig. 7.

	$k_{\text{bending},1} : k_{\text{bending},2}$	$k_{\text{axial},1} : k_{\text{axial},2}$	Nonlinear Coefficient (α)
$E_2 = 1$ MPa	0.54:1	120:1	790.2
$E_2 = 3$ MPa (polymer)	0.18:1	40:1	463.4
$E_2 = 15$ MPa	0.036:1	8:1	102.7
$E_2 = 25$ MPa	0.022:1	4.8:1	39.7
$E_2 = 60$ MPa	0.009:1	2:1	−242.1

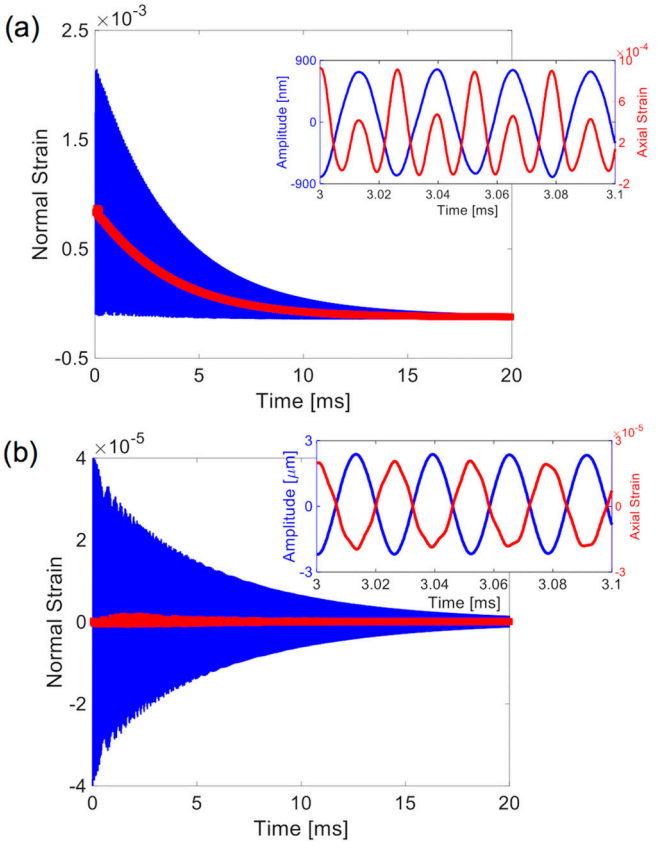

FIG. 8. (a) An axial strain response of the polymer component (in blue) and the average of axial strains per cycle (in red) at its midplane. The average normal strain is positive and increases as the oscillation amplitude increases, indicating that the polymer component is mainly in tension to be the source of Duffing nonlinearity at large amplitudes. The figure in the inset compares the axial strain response (in blue) with the vertical displacement (in red). It is clear that the frequency of polymer strain responses is twice of the displacement response. (b) An axial strain response of the silicon cantilever (in blue) and average of axial strains per cycle (in red) at its midplane. The figure represents that the average normal strains in the cantilever remain close to zero regardless of the amplitude of the oscillations. The figure in inset compares the axial strain response (in blue) with the time response (in red) at midplane of the silicon cantilever. It is shown that the frequency of strain responses is equal to the frequency of the displacement responses, proving that the cantilever dynamical behavior is almost linear.

We take advantage of the FE simulation to further investigate the dynamic response of the system and test the assumptions used in our analytical model. In Fig. 8, the blue curves plot the normal axial strains at the midplane of the polymer attachment (a) and the Si cantilever (b) as a function of the simulated time; the red curves plot the axial strains averaged per oscillation cycle. The notable difference between the Si cantilever and polymer attachment is that the Si cantilever experiences positive (tensile) and negative (compressive) axial strains over an oscillation cycle while the polymer attachment mainly undergoes tensile strain (i.e., axial stretching). As a result, the averaged axial strain over a cycle is almost zero for the Si component [cf. the red curve in Fig. 8(b)], regardless of the oscillation amplitudes, while that of polymer attachment is always positive and decreased with the decrease in the oscillation amplitude [cf. the red curve in Fig. 8(a)]. This trend is also clearly shown in the insets, displaying a few cycles of vertical displacement (blue) and axial strain (red) at the midplane of the polymer attachment and Si microcantilever, respectively. Assuming that the response obeys the general form of a harmonic response $y(t) = A\sin(\omega t)$, the axial strains in the Si microcantilever (e_1) and polymer attachment (e_2) are derived based on the aforementioned analytical model,

$$e_1 = \frac{\Delta L_1}{L_1} = \frac{A}{L_1}(\sin(\omega t))$$
$$e_2 = \frac{\Delta L_2}{L_2} = \frac{A^2}{4{L_2}^2}(1 - \cos(2\omega t)). \quad (5)$$

Equation (5) clarifies that the strain response in the Si microcantilever has the same frequency as the excitation frequency but becomes twice the excitation frequency in the polymer attachment, as we can confirm from the inset of Fig. 8. Also, note that the value of the axial strain is more than an order of magnitude smaller in the Si component compared with the axial strain in the polymer attachment while its vertical oscillation amplitude is higher due to the large difference of the axial stiffness between these two. This detailed interpretation of the FEA results validates the assumptions made in our analytical model. The vertical spring representing the Si cantilever experiences the compressive and tensile stresses when the mass oscillates vertically about the SEP, while the horizontal spring modeling the polymer attachment is under the tension only throughout the oscillation. As the theoretical model showed, this polymer attachment (i.e., horizontal spring) is the main source of geometric nonlinearity of this whole microcantilever-polymer system. It is worth noting again that this unique integration of intentional nonlinearity was achieved by implementing a largely dissimilar stiffness in the beam structural design via a sudden change of geometric parameters and material.

VI. CONCLUSION

In this paper, we integrate a nonlinear component (i.e., polymer) to an otherwise linear microcantilever to implement strong, geometric nonlinearity. It is found that the investigated Si microcantilever-polymer system exhibits a strong nonlinear behavior in the first three flexural modes. The comprehensive experimental, analytical, and numerical analyses were performed to investigate the nonlinear mechanism induced by the unique design of this nonlinear system. The deeper understanding we obtained in this paper offers a new strategy of tailoring the geometric nonlinearity based on the structural optimization of a nonprismatic, heterogeneous microbeam resonator.

ACKNOWLEDGMENTS

This paper was financially supported in part by Defense Advanced Research Projects Agency (Young Faculty Award D16AP00110). The contents of this paper are those of the authors and do not necessarily reflect the position or the policy of the government. We also acknowledge the Ohio Supercomputing Center for providing computational resources.

[1] W. Zhang, K. Hu, Z. Peng, and G. Meng, Sensors **15**, 26478 (2015).
[2] K. Jensen, K. Kim, and A. Zettl, Nat. Nanotechnol. **3**, 533 (2008).
[3] B. Lassagne, D. Garcia-Sanchez, A. Aguasca, and A. Bachtold, Nano Lett. **8**, 3735 (2008).
[4] N. Kacem, J. Arcamone, F. Perez-Murano, and S. Hentz, J. Micromech. Microeng. **20**, 045023 (2010).
[5] D. Berdy, B. Jung, J. Rhoads, and D. Peoulis, Sens. Actuators, A **188**, 148 (2012).
[6] U. Bartsch, J. Gaspar, and O. Paul, J. Micromech. Microeng. **20**, 035016 (2010).
[7] B. Mann and N. Sims, J. Sound Vibration **319**, 515 (2009).
[8] L. M. Jonsson, S. Axelsson, T. Nord, S. Viefers, and J. M. Kinarat, Nanotechnology **15**, 1497 (2004).
[9] S. W. Lee, D. S. Lee, R. E. Morjan, S. H. Jhang, M. Sveningsson, O. A. Nerushev, and E. E. Campbell, Nano Lett. **4**, 2027 (2004).
[10] A. Yao and T. Hikihara, Appl. Phys. Lett. **105**, 123104 (2014).
[11] H. Noh, S. Shim, M. Jung, Z. G. Khim, and J. Kim, Appl. Phys. Lett. **97**, 033116 (2010).
[12] M. A. Hafiz, L. Kosuru, and M. I. Younis, Nat. Commun. **7**, 11137 (2016).
[13] C. Zhao, X. Guo, Z. Liu, and M. Li, Micro Nano Lett. **8**, 614 (2013).
[14] D. Antonio, D. H. Zanette, and D. Lopez, Nat. Commun. **3**, 806 (2012).
[15] D. Antonio, D. A. Czaplewski, J. R. Guest, D. Lopez, S. I. Arroyo, and D. H. Zanette, Phys. Rev. Lett. **114**, 034103 (2015).
[16] M. H. Matheny, M. Grau, L. G. Villanueva, R. B. Karabalin, M. Cross, and M. L. Roukes, Phys. Rev. Lett. **112**, 014101 (2014).
[17] L. G. Villanueva, E. Kenig, R. B. Karabalin, M. H. Matheny, R. Lifshitz, M. C. Cross, and M. L. Roukes, Phys. Rev. Lett. **110**, 177208 (2013).
[18] S. Dou, B. S. Strachan, S. W. Shaw, and J. S. Jensen, Phil. Trans. R. Soc. A **373**, 0408 (2015).

[19] R. B. Karabalin, M. C. Cross, and M. L. Roukes, Phys. Rev. B **79**, 165309 (2009).
[20] H. Cho, M. Yu, A. F. Vakakis, L. A. Bergman, and D. M. Mcfarland, Nano Lett. **10**, 1793 (2010).
[21] W. J. Venstra, M. J. Capener, and S. R. Elliot, Nanotechnology **25**, 425501 (2014).
[22] L. G. Villanueva, R. B. Karabalin, M. H. Matheny, E. Kenig, and M. L. Roukes, Nano Lett. **11**, 5054 (2011).
[23] R. B. Karabalin, R. Lifshitz, M. C. Cross, S. C. Masmanidis, and M. L. Roukes, Phys. Rev. Lett. **106**, 094102 (2011).
[24] E. Kenig, M. C. Cross, R. Lifshitz, R. B. Karabalin, L. G. Villanueva, M. H. Matheny, and M. L. Roukes, Phys. Rev. Lett. **108**, 264102 (2012).
[25] E. Kenig, M. C. Cross, L. G. Villanueva, R. B. Karabalin, M. H. Matheny, R. Lifshitz, and M. L. Roukes, Phys. Rev. E **86**, 056207 (2012).
[26] A. Yao and T. Hikihara, Phys. Lett. A **377**, 2551 (2013).
[27] D. N. Guerra, A. R. Bulsara, W. L. Ditto, S. Sinha, K. Murali, and P. Mohanty, Nano Lett. **10**, 1168 (2010).
[28] M. Saghafi, H. Dankowicz, and W. Lacarbonara, Phil. Trans. R. Soc. A **471**, 20140969 (2015).
[29] S. Dou and J. S. Jensen, J. Sound Vibration **334**, 239 (2015).
[30] L. L. Li, P. M. Polunin, S. Dou, O. Shoshani, B. S. Strachan, J. S. Jensen, S. W. Shaw, and K. L. Turner, Appl. Phys. Lett. **110**, 081902 (2017).
[31] H. Cho, B. Jeong, M. Yu, A. F. Vakakis, D. M. Mcfarland, and L. A. Bergman, Int. J. Solids Struct. **49**, 2059 (2012).
[32] B. Jeong, H. Cho, H. Keum, S. Kim, D. M. Mcfarland, L. A. Bergman, W. King, and A. Vakakis, Nanotechnology **25**, 465501 (2014).
[33] B. Jeong, H. Cho, M. F. Yu, A. Vakakis, D. Mcfarland, and L. Bergman, ACS Nano **7**, 8547 (2013).
[34] Y. Zhang, J. H. Han, L. Zhu, M. Shannon, and J. Yeom, J. Micromech. Microeng. **24**, 115019 (2014).
[35] S. Peshin, K. Asadi, H. Cho, and J. Yeom (unpublished).